Cell Death & Differentiation

ARTICLE

Site-1 protease controls osteoclastogenesis by mediating LC3 transcription

Zeyu Zheng[1,2] · Xuyang Zhang[1,2] · Bao Huang[1,2] · Junhui Liu[1,2] · Xiaoan Wei[1,2] · Zhi Shan[1,2] · Hao Wu[3] · Zhenhua Feng[1,2] · Yilei Chen[1,2] · Shunwu Fan[1,2] · Fengdong Zhao ⬤[1,2] · Jian Chen ⬤[1,2]

Abstract

Site-1 protease (S1P) is a Golgi-located protein that activates unique membrane-bound latent transcription factors, and it plays an indispensable role in endoplasmic reticulum stress, lipid metabolism, inflammatory response and lysosome function. A patient with S1P mutation exhibits severe skeletal dysplasia with kyphoscoliosis, dysmorphic facial features and pectus carinatum. However, whether S1P regulates bone remodeling by affecting osteoclastogenesis remains elusive. Here, we show that S1P is indeed a positive regulator of osteoclastogenesis. S1P ablation in mice led to significant osteosclerosis compared with wild-type littermates. Mechanistically, S1P showed upregulated during osteoclastogenesis and was identified as a direct target of miR-9-5p. S1P deletion in bone marrow monocytes (BMMs) inhibited ATF6 and SREBP2 maturation, which subsequently impeded CHOP/SREBP2-complex-induced LC3 expression and autophagy flux. Consistently, transfection of LC3 adenovirus evidently rescued osteoclastogenesis in S1P-deficient BMMs. We then identified the interaction regions between CHOP and SREBP2 by Co-immunoprecipitation (Co-IP) and molecular docking. Furthermore, S1P deletion or inhibitor efficaciously rescued ovariectomized (OVX)- and LPS-induced bone loss in vivo. Collectively, we showed that S1P regulates osteoclast differentiation in a LC3 dependent manner and so is a potential therapy target for osteoporosis.

These authors contributed equally: Zeyu Zheng, Xuyang Zhang, Bao Huang

Edited by H-U Simon

✉ Fengdong Zhao
zhaofengdong@zju.edu.cn

✉ Jian Chen
chenjian-bio@zju.edu.cn

1 Department of Orthopaedic Surgery, Sir Run Run Shaw Hospital, Zhejiang University School of Medicine, Hangzhou, China

2 Key Laboratory of Musculoskeletal System Degeneration and Regeneration Translational Research of Zhejiang Province, Hangzhou, China

3 Department of Orthopaedics and Traumatology, The University of Hong Kong, Pokfulam, Hong Kong SAR, China

Introduction

Bone has many essential functions such as haemopoiesis, protecting organs, and secreting hormones. Resident osteoclasts (OCs), osteoblasts (OBs) and osteocytes are involved in a continuous remodeling process to maintain function [1], and dysfunction in osteoclasts can cause osteoporosis, osteosclerosis and osteoarthritis [2–4]. As human longevity increases, the number of osteoporotic fractures is expected to reach 6.3 million by 2050 [5]. Hence, understanding the mechanisms of osteoclast differentiation is critical.

Autophagy is a biological process that degrades and recycles metabolites and organelles in order to maintain homeostasis [6]. It is a highly organized degradation program which includes the activation of the ULK1 (unc-51 like kinase 1) complex, ATG (autophagy related) proteins and MAP1LC3B (microtubule associated protein 1 light chain 3 beta, LC3)-II installation, and the maturation of autophagosomes [7]. Autophagy plays an essential role in osteoclastogenesis. Hypoxia and endoplasmic reticulum (ER) stress can induce autophagy activation to promote

osteoclast differentiation [8, 9]. The autophagy-related proteins ATG5, ATG7, ATG4B and LC3 also play critical roles in osteoclast resorption [10]. ATG4B deficiency affects LC3 conversion and blocks both resorptive activity and CTSK (cathepsin K) expression. When LC3 was knocked down, actin ring formation, resorption activity, and CTSK release were all inhibited [11]. ATG7 knockout and the autophagy inhibitor chloroquine can rescue bone loss in ovariectomized mice [12]. In a model of osteoarthritis, TNF-α induced increases in Atg7 and Beclin-1 led to enhanced osteoclastogenesis and bone-resorption activities [13]. All these studies showed that autophagy is closely associated with osteoclast formation and function under both normal and pathological states.

Site-1 protease (S1P) is encoded by membrane-bound transcription factor peptidase, site 1 (MBTPS1). S1P is located in the Golgi, and activates unique membrane-bound latent transcription factors sequentially with the site-2 protease (S2P). ATF6 and SREBPs are representative transcription factors which can be activated by S1P [14, 15]. Mice with global deficiency of S1P have embryonic lethality prior to implantation during embryogenesis [16]. Mice with osteoblast-or chondrocyte-specific deletion of S1P exhibit skeletal dysplasia and die during or shortly after birth [17, 18]. Also, S1P is required for ECM signaling and axial elongation during somitogenesis and vertebral development [17]. Patient with S1P mutation exhibits skeletal dysplasia with kyphoscoliosis, dysmorphic facial features and pectus carinatum [19]. However, how is S1P expression regulated in osteoclasts and whether S1P deficiency leads to skeletal abnormality by affecting osteoclastogenesis remains unclear.

In this study, we found S1P was upregulated during osteoclastogenesis and was directly targeted by miR-9-5p. Two mice models with osteoclasts-specific S1P knockout which showed significantly increased bone mass compared with wild-type littermates. S1P inhibitor (PF429242) efficaciously rescued ovariectomized (OVX)- and LPS-induced bone loss in vivo. We showed that ATF6/CHOP/LC3 and SREBP2/LC3 pathways are critical for the function of S1P in osteoclasts.

Results

S1P plays a positive role in osteoclastogenesis

To investigate S1P protein expression in OCs, we used murine bone marrow monocytes (BMMs) and human peripheral blood monocytes (PBMs), which are widely used as primary osteoclast precursors, to induce OCs with M-CSF and RANKL. Similar with NFATC1, S1P protein expression was upregulated in a time-dependent manner with the

stimulation of RANKL (Fig. 1A, B and Supplementary Fig. S1A, B). The expression of S1P was further detected in the OVX-induced osteoporosis model. We found although S1P mRNA was not significantly elevated with RANKL stimulation, S1P protein expression was increased. Consistently, more expression and colocalization of S1P and ACP5 were found in the OVX group by immunofluorescence staining (Fig. 1C and Supplementary Fig. S1C–E). Also, S1P and ACP5 immunofluorescence staining showed similar results in collagen induced arthritis (CIA) model (Supplementary Fig. S1F). We then investigated the role of S1P in osteoclastogenesis and found that S1P deficiency impeded osteoclast formation (Fig. 1D, E), and resorption function (Supplementary Fig. S1G, H). The results were further confirmed by the fact that osteoclasts formation following a S1P inhibitor (PF429242) treatment were significantly inhibited in a dose-dependent manner both in murine BMMs and human PBMs (Supplementary Figs. S1I, J and S2A–C). Consistently, the elevated expression of osteoclast related-genes including DC-stamp, NFACT1, TRAP, CTSK and c-Fos were inhibited in the S1P knockout group compared with the WT group when BMMs were cultured with M-CSF and RANKL for 5 days (Supplementary Fig. S2D). Moreover, we detected the effect of S1P overexpression on osteoclastogenesis via adenovirus transfection. Compared with the control group, the S1P overexpression group formed osteoclasts with more nuclei (Fig. 1F, G) and showed a greater absorption area (Supplementary Fig. S2E, F). Considering that S1P and S2P work sequentially in the Golgi, we detected the potential role of S2P in osteoclastogenesis. We found no significant change of S2P expression during osteoclast formation, and that knocked-down S2P by siRNA had little effect on osteoclast formation (Supplementary Fig. S2G–J). These results suggest that S1P might play a positive role in osteoclastogenesis.

Conditional knockout of S1P causes osteosclerosis in mice

According to a previous study, the LysM-Cre-Flox model deletes the target gene in the osteoclast precursors, while the CTSK-Cre-Flox model works at a late stage of osteoclast differentiation [20]. To further investigate the role of S1P in osteoclast formation and activity, we generated LysM-Cre-S1P$^{f/f}$ and CTSK-Cre-S1P$^{f/f}$ conditional knockout (cKO) mice. Three-month-old LysM-Cre-S1P$^{f/f}$ and CTSK-Cre-S1P$^{f/f}$ mouse femurs were harvested to detect bone mass. Quantitative microtomography (micro-CT) analysis showed that LysM-Cre-S1P$^{f/f}$ mice exhibited a 3.1-fold increase in bone volume/tissue volume (BV/TV), a 1.3 fold increase in trabecular number (Tb.N), a 33% decrease in trabecular spacing (Tb.Sp), and a 1.3 fold increase in trabecular
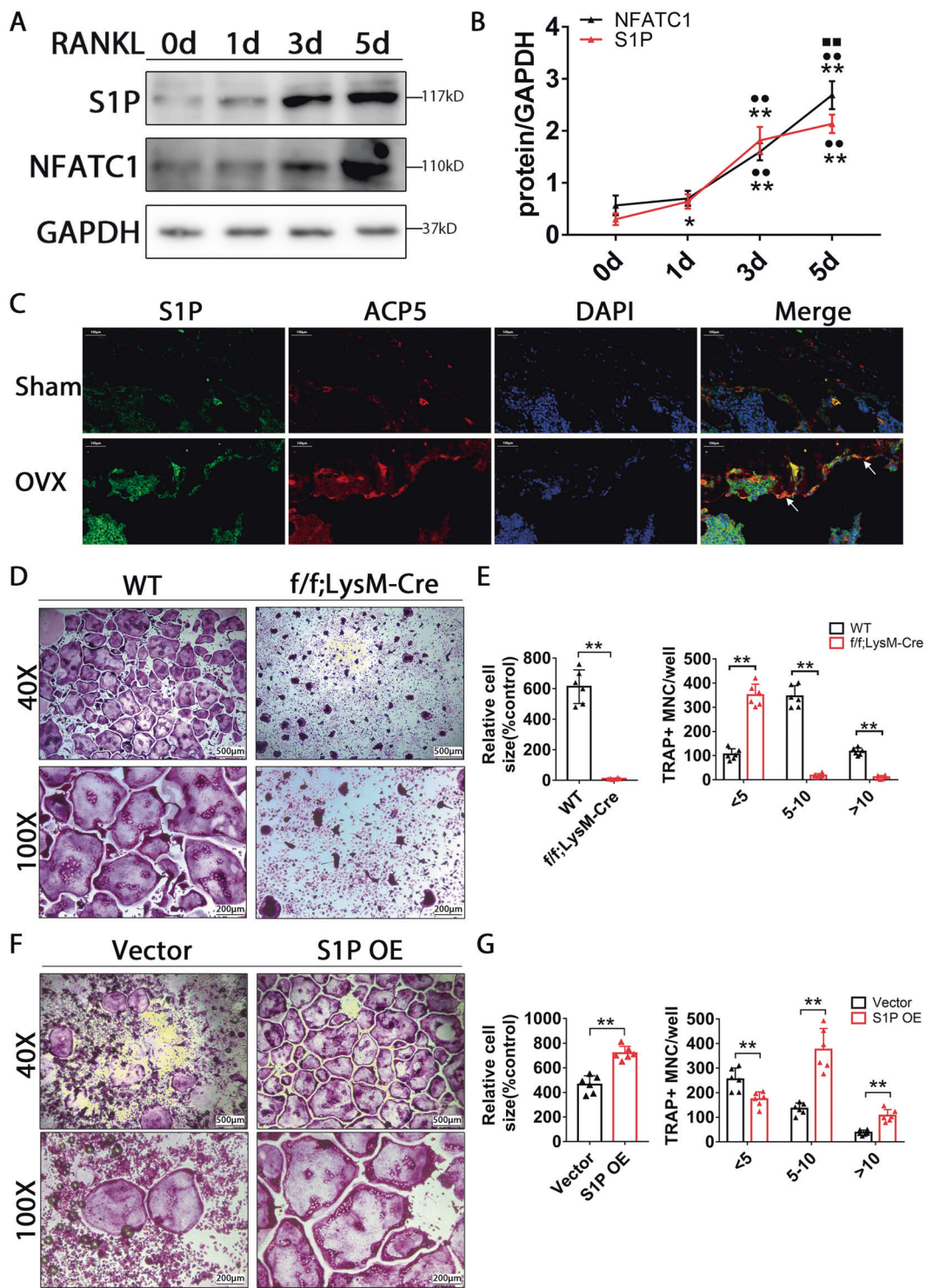
Fig. 1 S1P plays a positive role in osteoclastogenesis. A, B Protein expression of S1P and NFATC1 in BMMs under the treatment of M-CSF and RANKL(*, compared with 0d; ●, compared with 1d; ■, compared with 3d. The symbols above represent the statistics of NFATC1 and the symbols below represent S1P.); ($n = 3$). **C** S1P (green) and ACP5 (red) immunofluorescence of femur sections from sham and OVX mice; The arrow indicates the cells which express both S1P and ACP5; Scale bars, 100 μm. **D** TRAP staining to detect osteoclastogenesis of BMMs from WT (wild-type) and LysM-Cre-S1P$^{f/f}$ mice; 40×, Scale bars, 500 μm; 100×, Scale bars, 200 μm.

E Quantification of size and nuclei numbers of TRAP-positive multinuclear cells ($n = 6$). **F** TRAP staining to detect osteoclastogenesis of BMMs following the lentivirus transduction of pLenti-EF1a-S1P or the empty vector; 40×, Scale bars, 500 μm; 100×, Scale bars, 200 μm. **G** Quantification of size and nuclei numbers of TRAP- positive multinuclear cells ($n = 6$). Data are presented as mean ± SD. *$P < 0.05$, **$P < 0.01$. n value means the number of repetitions in each independent experiment. Each experiment was performed at least three times.
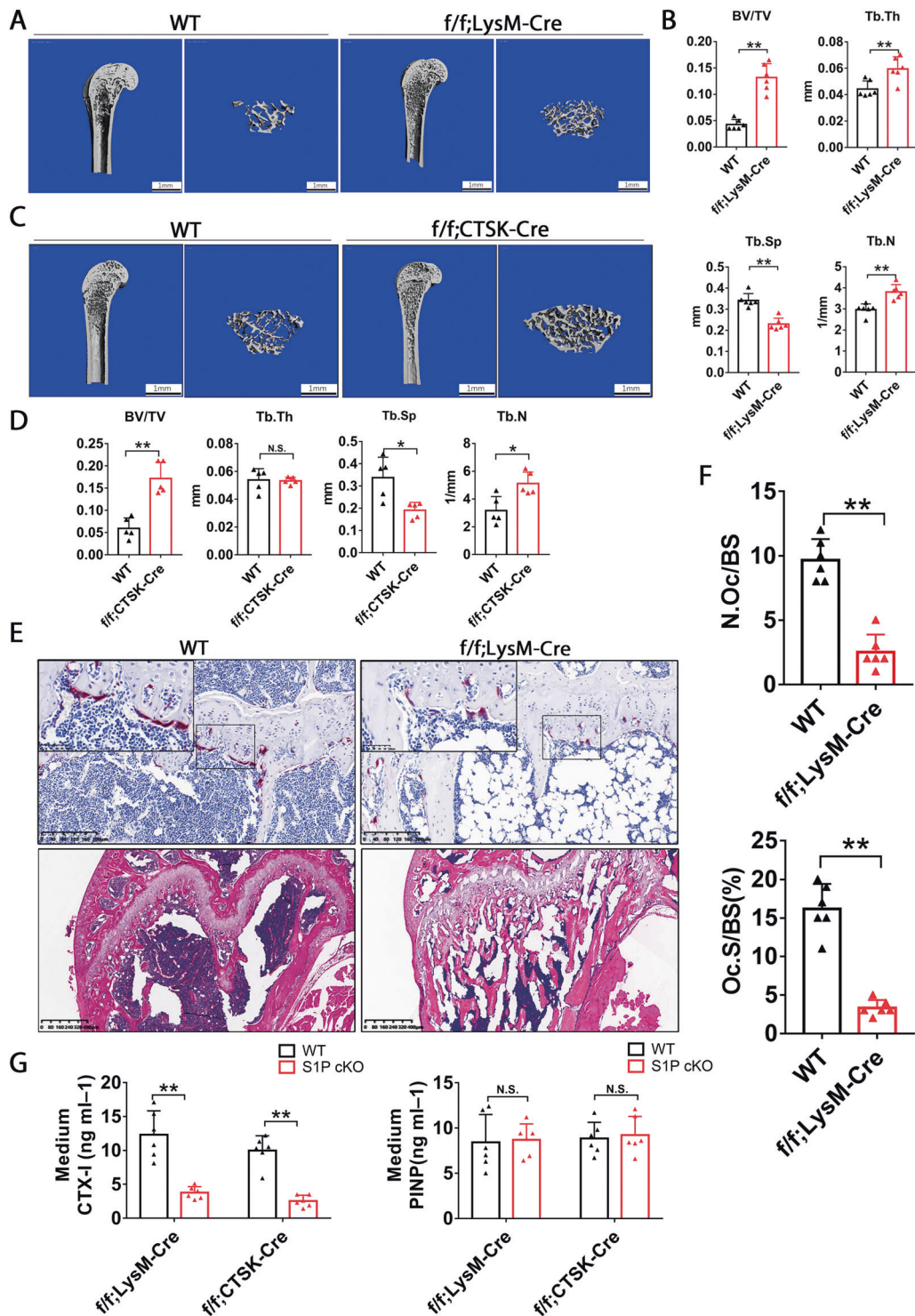
thickness (Tb.Th) compared with wild-type littermates (Fig. 2A, B). Similarly, micro-CT showed that bone mass was increased in CTSK-Cre-S1P$^{f/f}$ mice (Fig. 2C, D). TRAP staining showed that LysM-Cre-S1P$^{f/f}$ mice had fewer osteoclasts on trabecular surfaces of the femur compared with wild-type littermates (Fig. 2E). Histomorphometric parameters of femurs showed a 4.6-fold decrease in

osteoclast numbers per bone surface (N.Oc/BS) and a 4.8-fold decrease in osteoclast covered surface per bone surface (Oc.S/BS) compared with wild-type littermates in the LysM-Cre-S1P$^{f/f}$ trabecular bone area (Fig. 2F). CTSK-Cre-S1P$^{f/f}$ mice displayed the same tendency as LysM-Cre-S1P$^{f/f}$ mice (Supplementary Fig. S3A, B). Hematoxylin-eosin (H&E) staining demonstrated that skeletal mass was increased, and

◄ **Fig. 2 Conditional knockout of S1P causes osteosclerosis in mice. A** Micro-CT and three-dimensional (3D) reconstruction images of the distal femur trabeculae of 3-month-old WT and LysM-Cre-S1P^f/f mice are shown; Scale bars, 1 mm. **B** Quantification of bone volume/tissue volume (BV/TV), trabecular number (Tb.N), trabecular separation (Tb.Sp) and trabecular thickness (Tb.Th) ($n = 6$). **C** Micro-CT and three-dimensional (3D) reconstruction images of the distal femur trabeculae of 3-month-old WT and CTSK-Cre-S1P^f/f mice are shown; Scale bars, 1 mm. **D** Quantification of bone volume/tissue volume (BV/TV), trabecular number (Tb.N), trabecular separation (Tb.Sp) and trabecular thickness (Tb.Th) ($n = 5$). **E** TRAP staining and H&E staining of 3-month-old WT and LysM-Cre-S1P^f/f mice femurs; TRAP staining, Scale bars, 200 μm; H&E staining, Scale bars, 400 μm. **F** Quantification of N.Oc/BS (osteoclast number/bone surface) and the percentage of osteoclast surface per bone surface (Oc.S/BS(%)) ($n = 6$). **G** Medium CTX-I (C-terminal telopeptide of type I collagen) and PINP (Procollagen I N-Terminal Propeptide) concentration measured by ELISA from LysM-Cre-S1P^f/f, CTSK-Cre-S1P^f/f and their WT littermates ($n = 6$). Data are presented as mean ± SD. *$P < 0.05$, **$P < 0.01$. n value means the number of mice in each experiment.

bone marrow cavities were obviously narrowed in S1P cKO mice (Fig. 2E and Supplementary Fig. S3A). The circulating bone resorption marker C-terminal telopeptide of type I collagen (CTX-I) was decreased and the bone formation marker procollagen I N-Terminal propeptide (PINP) displayed no change in the serum from the LysM-Cre-S1P^f/f and CTSK-Cre-S1P^f/f mice (Fig. 2G). These results showed that osteoclast-specific S1P deletion damaged the osteoclastogenesis leading to osteosclerosis in vivo.

S1P is directly regulated by miR-9-5p in osteoclasts

As mentioned above, S1P protein expression was upregulated both under RANKL treatment and in OVX mice (Fig. 1A and Supplementary Fig. S1A–D). However, the S1P mRNA expression showed no significant change in osteoclasts (Fig. 3A and Supplementary Fig. S1C). In order to explore the mechanism of how S1P protein is upregulated, we treated BMMs with the protein synthesis inhibitor cycloheximide (CHX). RANKL failed to relieve S1P downregulated caused by CHX treatment, indicating that S1P isn't regulated at post-translation process (Fig. 3B, C). Therefore, we considered miRNAs might regulate the S1P expression in osteoclasts, and predicted the S1P-targeted miRNAs by Targetscan and miRDB databases (Fig. 3D). The selected 8 overlapped miRNAs were detected in the process of osteoclasts induction and only miR-9-5p showed gradually decreased in a time-dependent manner (Fig. 3E). What's more, it was reported that miR-9 played important role in osteoclasts and rheumatoid arthritis [21, 22]. We transfected the miR-9-5p inhibitor and mimic in BMMs and found the inhibitor could upregulate S1P and NFATC1 protein expression while the mimic downregulated the two proteins expression (Fig. 3F, G). We then conducted the luciferase reporter plasmids containing the 3′UTR-WT or 3′

UTR-MUT of S1P. Dual luciferase reporter assay revealed that miR-9-5p mimic significantly decreased the luciferase activity in the cells transfected with 3′UTR-WT plasmid, but the effect was abrogated when transfected with 3′UTR-MUT plasmid (Fig. 3H, I). These results showed S1P was a direct target of miR-9-5p in osteoclasts.

S1P controls osteoclastogenesis by mediating the ATF6/CHOP/LC3 pathway

S1P is known to activate unique membrane-bound latent transcription factors, such as ATF6, to affect genes expression and to mediate intracellular physiological processes. ATF6 is a key factor in ER stress, apoptosis and autophagy which are biological processes closely associated with osteoclastogenesis [14]. Therefore, we speculated that lack of S1P would damage osteoclast differentiation by impeding ATF6 cleaving. To verify our hypothesis, we first examined the effect of S1P deficiency on ER stress. The data showed that S1P, ATF6 maturation (m-ATF6) and CHOP were severe decreased in S1P-deficient osteoclasts, whereas most other ER stress-related proteins, such as PERK, XBP-1, ATF4 and BIP, EDEM1, DNAJB9 and CANX showed no significant changes or mild decreased (ERN1) (Fig. 4A, B and Supplementary Fig. S4A, B). This implies that S1P deficiency had little impact on ER stress. Next, we considered that knockout of S1P might damage osteoclastogenesis by influencing apoptosis, since ATF6/CHOP is associated with cell viability [23, 24]. However, the Cell Counting Kit-8 assay showed no difference in cell proliferation between the wild-type and LysM-Cre-S1P^f/f groups. PE Annexin V apoptosis detection showed that S1P deficiency only downregulated BMMs early apoptosis slightly under RANKL treatment, which can hardly account for the impeded osteoclast formation with S1P deficiency (Supplementary Fig. S4C–E). Then we detected the impact of S1P deficiency on autophagy. Intriguingly, the autophagy flux was damaged in the S1P-deficient group as indicated by LC3-GFP-RFP indicator, immunofluorescence of LC3, as well as protein expression of LC3 and SQSTM1 (Fig. 4C–E and Supplementary Fig. S4F). To investigate the potential mechanism of how S1P regulates autophagy, the expression of autophagy-related genes was detected. We found that most genes were upregulated in either the wild-type or S1P-deficient groups following RANKL treatment, except LC3. As shown, RANKL treatment upregulated LC3 in the wild-type group, but decreased it in the S1P-deficient group, which displayed the similar expression tendency with S1P (Supplementary Fig. S4G, H). This result suggested that S1P downstream signaling might directly regulate LC3 transcription. LC3 is the key factor for osteoclasts' actin ring formation, CTSK release and resorption activity [10, 11], which suggests that osteoclast
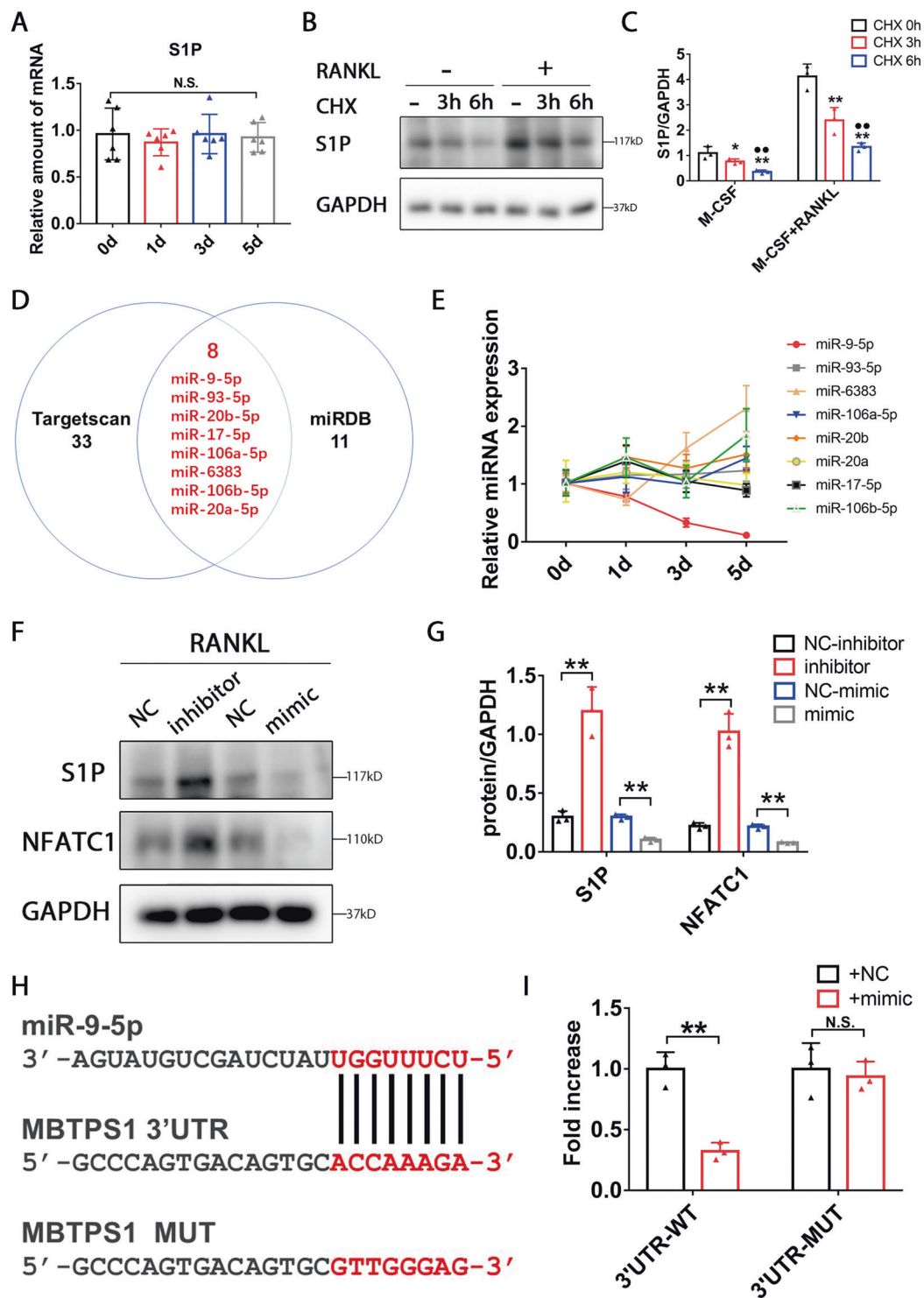
Fig. 3 S1P is directly regulated by miR-9-5p in osteoclasts. A The mRNA level of S1P during osteoclastogenesis. **B, C** Protein expression of S1P in BMMs with or without RANKL under cycloheximide (CHX) treatment ($n = 3$). **D** The predicted result of the S1P-targeted miRNAs by Targetscan and miRDB databases. **E** The level of selected 8 overlapped miRNAs in the process of osteoclasts induction ($n = 3$). **F, G** Protein expression of S1P and NFATC1 in BMMs transfected with mimic or inhibitor of miR-9-5p under RANKL treatment ($n = 3$). **H** The sequence of 3′UTR-WT or 3′UTR-MUT of S1P. **I** 3′UTR-WT or 3′UTR-MUT of S1P activity were analyzed by luciferase assay in HEK293 cells ($n = 3$). Data are presented as mean ± SD. *$P < 0.05$, **$P < 0.01$. n value means the number of repetitions in each independent experiment. Each experiment was performed at least three times.
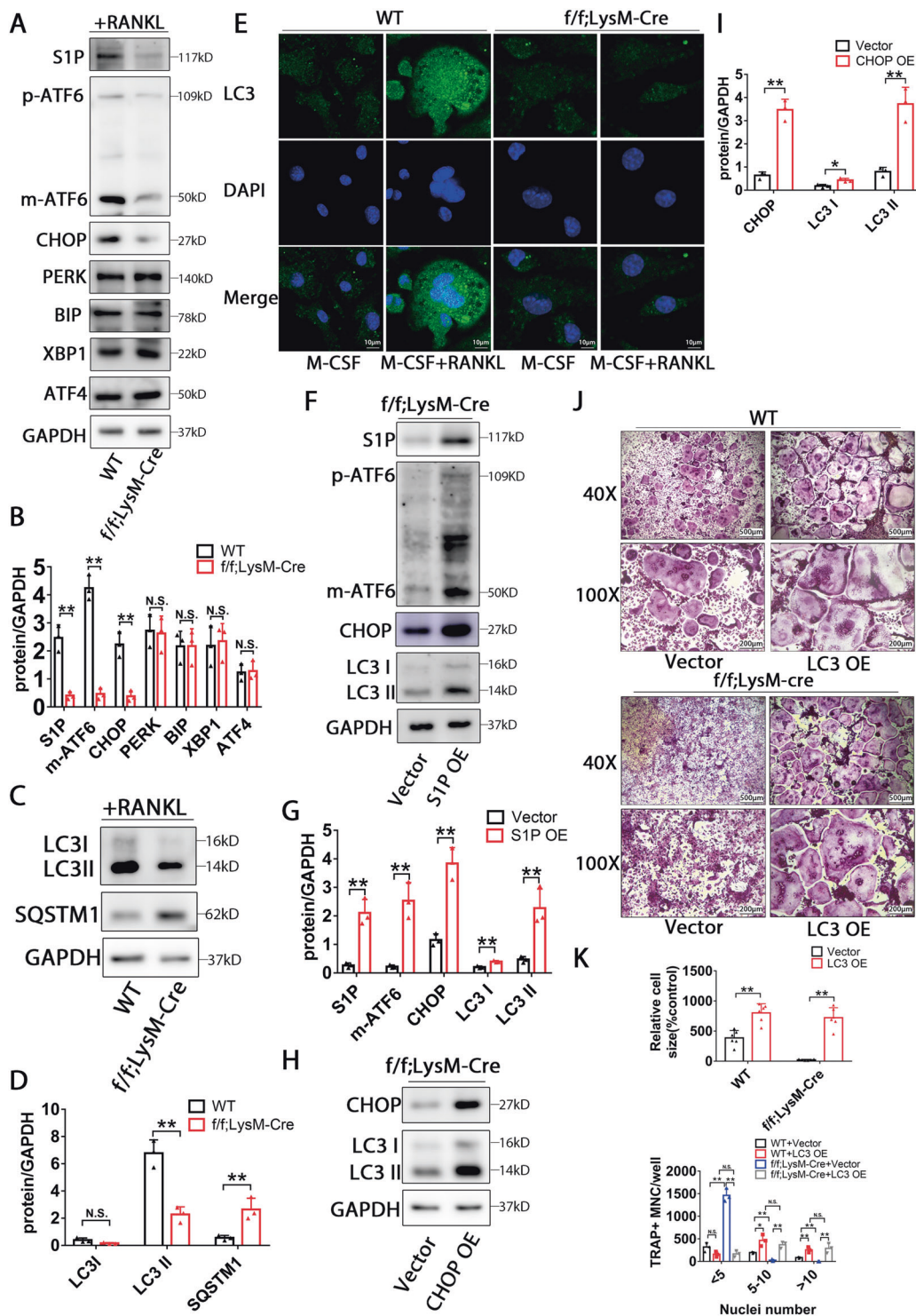
abnormality following S1P knockout is LC3 dependent. It has been reported that cleaved ATF6 can promote CHOP expression, which upregulates the transcription of LC3 by directly binding to the promoter [24]. Therefore, we considered that S1P controls osteoclastogenesis by mediating the ATF6/CHOP/LC3 pathway. To this end, m-ATF6 was overexpressed in S1P-deficient BMMs. CHOP and LC3

protein and osteoclasts maker gene such as NFATC1, c-Fos and TRAP were recused compared with vector group under RANKL treatment (Supplementary Fig. S5A–C). We then found CHOP expression was decreased in the femur of LysM-Cre-S1P$^{f/f}$ mice (Fig. S5D), and S1P or CHOP overexpression evidently increased the LC3 protein and mRNA expression (Fig. 4F–I and Supplementary Fig. S5E).

◀ **Fig. 4 S1P controls osteoclastogenesis by mediating ATF6/CHOP/LC3 pathway. A**, **B** Protein expression of S1P, ATF6 precursor (p-ATF6), ATF6 maturation (m-ATF6), CHOP, PERK, BIP, XBP1 and ATF4 in BMMs of WT and LysM-Cre-S1P$^{f/f}$ mice under the treatment of M-CSF and RANKL ($n = 3$). **C**, **D** Protein expression of LC3I, LC3II and SQSTM1 in BMMs of WT and LysM-Cre-S1P$^{f/f}$ mice under the treatment of M-CSF and RANKL ($n = 3$). **E** Confocal images of LC3 immunofluorescence of BMMs of WT and LysM-Cre-S1P$^{f/f}$ mice with or without RANKL treatment; Scale bars, 10 μm. **F**, **G** Protein expression of S1P, p-ATF6, m-ATF6, CHOP, LC3I and LC3II in BMMs of LysM-Cre-S1P$^{f/f}$ mice following the lentivirus transduction of pLenti-EF1a-S1P or the empty vector ($n = 3$). **H**, **I** Protein expression of CHOP, LC3I and LC3II in BMMs of LysM-Cre-S1P$^{f/f}$ mice following the lentivirus transduction of pLenti-EF1a-CHOP or the empty vector ($n = 3$). **J** TRAP staining to detect osteoclastogenesis of BMMs of WT or LysM-Cre-S1P$^{f/f}$ mice following the lentivirus transduction of pLenti-EF1a-LC3 or the empty vector; 40×, Scale bars, 500 μm; 100×, Scale bars, 200 μm. **K** Quantification of size and nuclei numbers of TRAP-positive multinuclear cells ($n = 6$). Data are presented as mean ± SD. *$P < 0.05$, **$P < 0.01$. n value means the number of repetitions in each independent experiment. Each experiment was performed at least three times.

Consistently, transfection of LC3 promoted wild-type, and rescued LysM-Cre-S1P$^{f/f}$ BMMs' osteoclastogenesis, which showed increased osteoclast size, nuclei numbers and TRAP + cells (Fig. 4J, K). These results suggest that S1P regulates osteoclastogenesis by mediating the ATF6/CHOP/LC3 pathway.

S1P/SREBP2 regulates LC3 transcription

As mentioned above, SREBP2 is also a representative transcription factor activated by S1P. Inhibiting SREBP2 suppresses RANKL-mediated osteoclastogenesis and prevents OVX-induced bone loss [25, 26]. In addition, SREBP2 is closely associated with autophagy and affects autophagy-related genes expression, but the mechanism remains unclear [27]. We speculated that S1P deficiency impedes SREBP2 activation leading to suppressed LC3 expression and damaged osteoclastogenesis. As expected, SREBP2 maturation (m-SREBP2) was decreased in the S1P-deficient group (Supplementary Fig. S6A, B). mRNA expression of LC3 was decreased in BMMs following SREBP2 knockdown, and increased in the SREBP2 over-expressed group (Fig. 5A). Overexpression of SREBP2 maturation obviously rescued LC3 protein level in S1P-deficient BMMs (Fig. 5B, C). In addition, Fatostatin, an inhibitor of SREBP2, impeded osteoclast formation while inhibiting LC3 expression (Supplementary Fig. S6C–F). Next, we focused on the mechanism of SREBP2 regulated LC3 transcription. The database (JASPAR: http://jaspar.genereg.net) predicted that the promoter region of LC3 had 8 putative binding sites for SREBP2. We generated 4 constructs derived from the 2000bp promoter fragment of LC3 which contain various putative transcriptional binding

sites (Fig. 5D). We found SREBP2 induced robust luciferase activity from P4 (−869 to −1bp), demonstrating it is the active promoter fragment (Fig. 5E). We then performed ChIP assay in BMMs treated with or without RANKL. As shown in Fig. 5F, SREBP2 increasingly bind to the site of −869 to −714bp following RANKL treatment, while other binding sites showed no obviously elevated. Furthermore, to confirm the functional binding site, we introduced mutations in the putative SREBP2-binding site of promoter fragments (P0 mut1, P0 mut2, P4 mut1 and P4 mut2), and observed that P0 and P4 mutant constructs decreased luciferase activity (Fig. 5G, H). These results suggested SREBP2 acted as a transcription factor of LC3.

CHOP and SREBP2 form a complex to regulate LC3 transcription synergistically

As we found CHOP and SREBP2 are both transcription factors of LC3, we speculated they formed a complex to promote LC3 transcription. To examine this possibility, we performed immunofluorescence staining of CHOP and SREBP2 in BMMs treated with or without RANKL. Confocal images displayed that CHOP and SREBP2 had more nuclear translocation and colocalization in the osteoclast-induced group (Fig. 6A). We then transfected Flag-SREBP2 and Myc-CHOP in HEK-293T cells for 2 days. Co-immunoprecipitation analyses showed that Flag-SREBP2 interacted with Myc-CHOP (Fig. 6B). To further probe the complex form with endogenous proteins in osteoclasts, we performed co-immunoprecipitation analyses in BMMs with or without RANKL stimulation. CHOP–SREBP2 interaction was enhanced with RANKL treatment (Supplementary Fig. S6G). To map the crucial domains of CHOP and SREBP2 that are responsible for their interaction, we generated different truncated fragments of m-SREBP according to Uniprot (S1–S5). Then we transfected the 5 fragments separately with CHOP in HEK-293T cells. S3 and S5 showed interaction with CHOP, suggesting Glutamine (Gln)-rich and Leucine-zipper (LZIP) regions of SREBP2 are required for the interaction (Fig. 6C). Also, we constructed 3 fragments of CHOP (C1–C3). The C3 fragment which containing basic motif and Leucine zipper (bZIP) region is essential for CHOP binding to SREBP2 (Fig. 6D). To gain further insights into the interaction between CHOP and SREBP2, CHOP was docked with naturally binding sites of SREBP2. In the complex obtained by molecular docking, CHOP stretches along the surface formed by two α-helices in chain A and chain B respectively (Fig. 6E). Notably, Chop forms a protruding negative electrostatic potential surface, which embedding itself in the positive electrostatic potential groove formed in the center of SREBP2 (Fig. 6F). As shown in Fig. 6G, a stable hydrogen-bonding network may greatly promote the CHOP binding
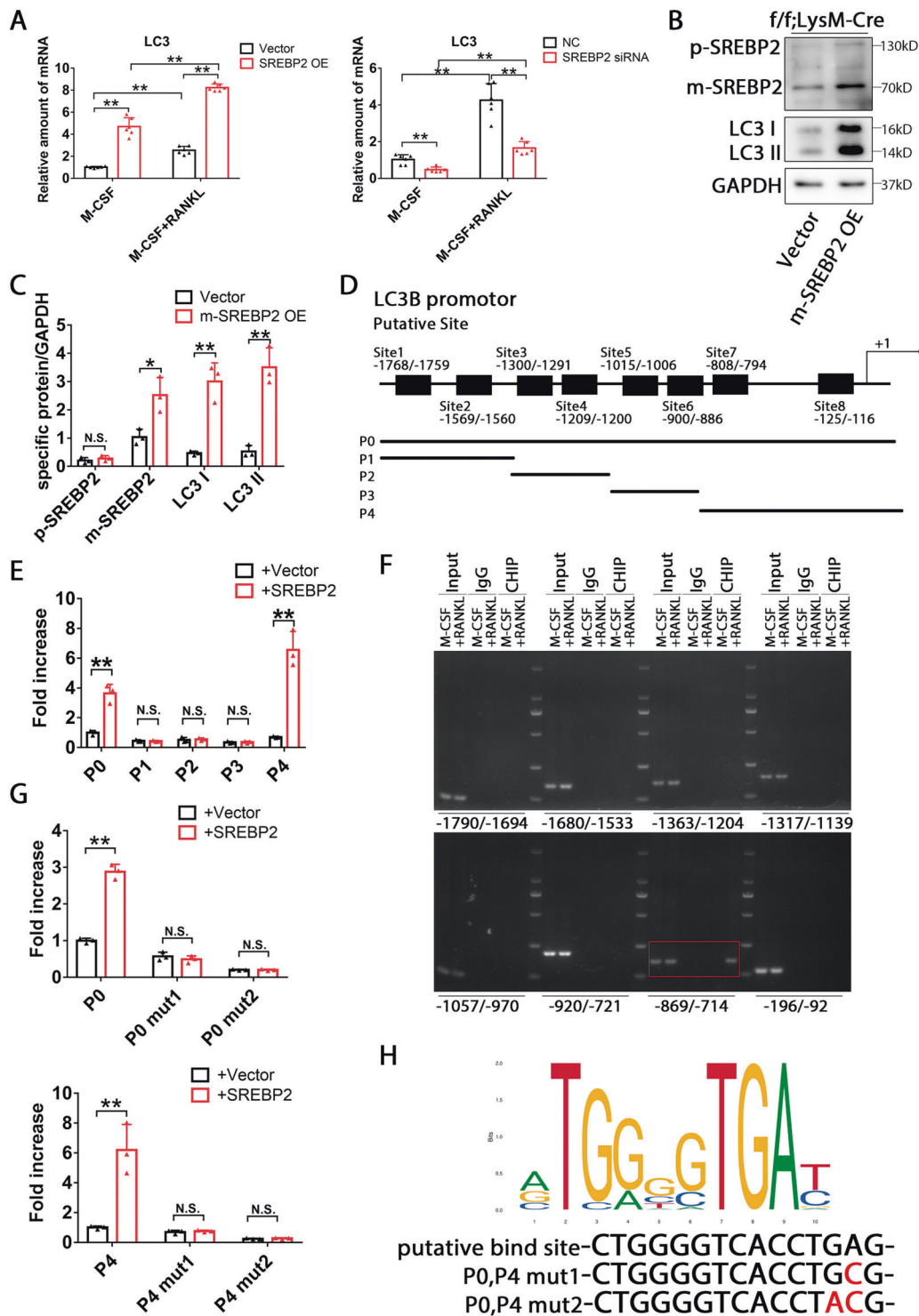
Fig. 5 S1P/SREBP2 regulates LC3 transcription. A The mRNA level of LC3 in BMMs following transduction of SREBP2 siRNA or pLenti-EF1a-SREBP2 in the presence or absence of RANKL ($n = 6$). **B**, **C** Protein expression of SREBP2 precursor (p-SREBP2), SREBP2 maturation (m-SREBP2), LC3I and LC3II in BMMs of LysM-Cre-S1P$^{f/f}$ mice following the transduction of pLenti-EF1a-m-SREBP2 or the empty vector ($n = 3$). **D** Putative SREBP2-binding sites within the 2000 bp region of LC3 promoter. **E** LC3 promoter activity was analyzed by luciferase assay in HEK293 cells ($n = 3$). **F** SREBP2 ChIP assay for the LC3 promoter. **G** P0, P4 and its mutant activity was analyzed by luciferase assay in HEK293 cells ($n = 3$). **H** Mutation in the putative SREBP2-binding site of the P0, P4 fragment. Data are presented as mean ± SD. *$P < 0.05$, **$P < 0.01$. n value means the number of repetitions in each independent experiment. Each experiment was performed at least three times.
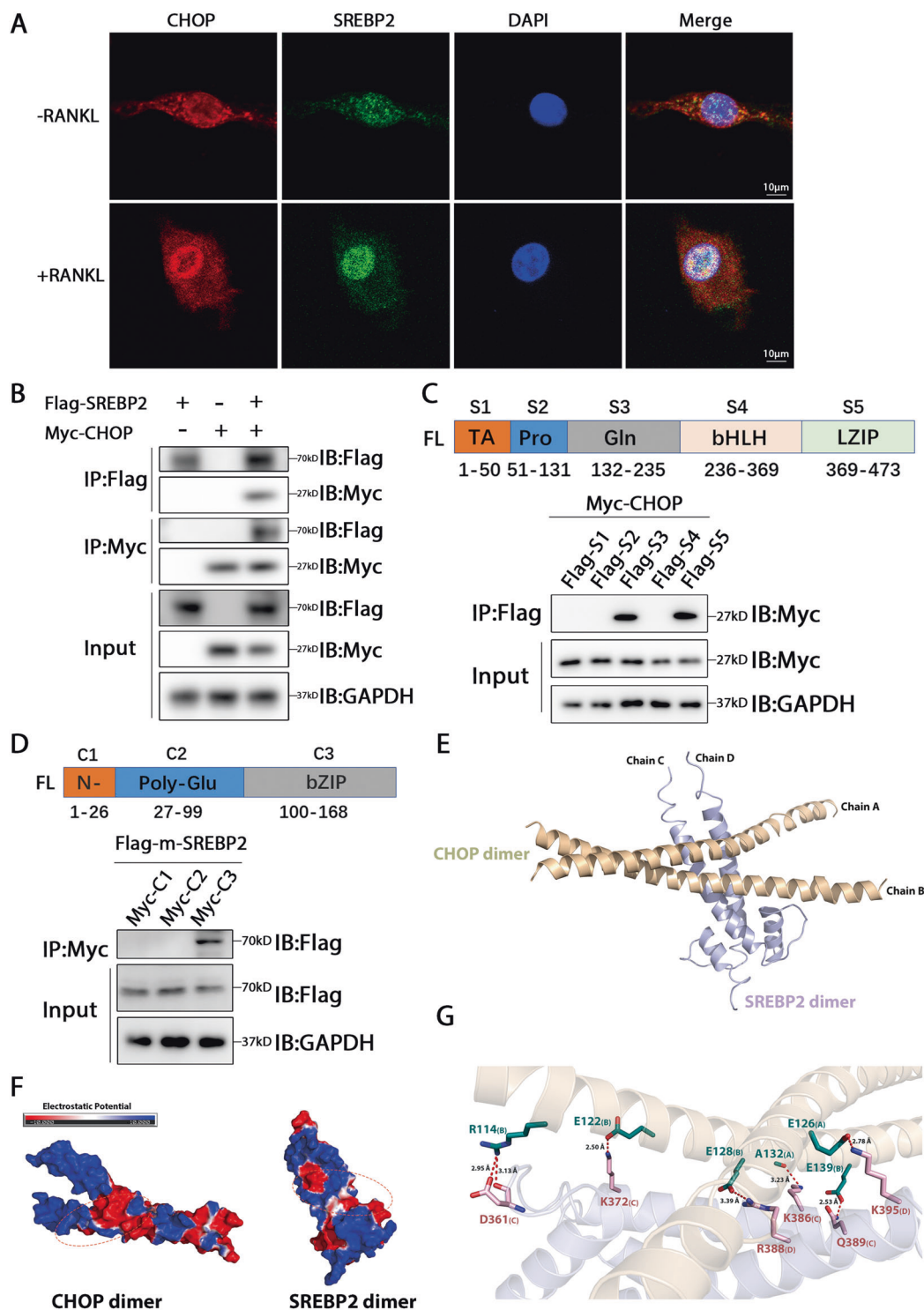
of SREBP2. The six residue pairs between CHOP and SREBP2 that formed important hydrogen-bonding interactions were identified as key residues. Intriguingly, the key residues of CHOP (R114, E122, E126, E128, A132, E139) were enriched in bZIP domain (100–147), while the key residues (D361, K372, K395, R388, K386, Q389) were main enriched in LZIP domain of SREBP2 (380–401).

These results indicated that bZIP domain in CHOP and LZIP domain in SREPB2 were critical for their interaction. Unfortunately, we failed to develop the structure of SREBP2 S3 region by homology modeling for it shares a low homology (<30%) with known proteins in RCSB PDB database, and the intact crystal structure data of SREBP2 remains unclear. It has been reported that CHOP bind to

◀ **Fig. 6 CHOP and SREBP2 form a complex to regulate LC3 transcription synergistically. A** Confocal images of CHOP (red) and SREBP2 (green) immunofluorescence of BMMs with or without RANKL treatment; Scale bars, 10 μm. **B** HEK293T cells were transfected with Flag-SREBP2, Myc-CHOP or Flag-SREBP2 and Myc-CHOP. Flag immunoprecipitates and Myc immunoprecipitates were analyzed by immunoblotting as outlined. **C** Full-length and various truncated fragments of SREBP2. S1, transcriptional activation (TA) region; S2, Proline (Pro)-rich region; S3, Glutamine (Gln)-rich region; S4, basic helix (bHLH) region; S5, Leucine zipper region. S1–S5 and CHOP plasmids were co-transfected in HEK293T cells. The interactions were detected through the indicated IP and IB analyses. **D** Full-length and various truncated fragments of CHOP. C1, N -terminal region; C2, Poly-Glutamic acid (Glu) region; C3, basic motif and Leucine zipper (bZIP) region. C1–C3 and m-SREBP2 plasmids were co-transfected in HEK293T cells. The interactions were detected through the indicated IP and IB analyses. **E** Overall structure of CHOP dimer bound to SREBP2 dimer in cartoon view. CHOP and SREBP2 are colored in wheat, light blue respectively, and the chain identifiers of each protein are labeled. **F** Computed electrostatic potentials of CHOP dimer and SREBP2 dimer. **G** Detailed interaction network between CHOP dimer and SREBP2 dimer. Key residues of CHOP (deep teal) and SREBP2 (pink) are displayed as sticks and the chain identifiers of residues are showed. H-bonds are displayed in red dash lines and the distances (acceptor to donor heavy atom) of H-bonds are labeled.

−253 to −99bp of LC3 promoter [24], which is contained in our P4 fragment. We found CHOP indeed elevated the luciferase activity of P0 and P4 fragments. Moreover, co-transfection of CHOP and SREBP2 showed the highest luciferase activity implying they acted synergistically (Supplementary Fig. S6H). All these data suggested that SREBP2 and CHOP formed a complex and acted synergistically to regulated LC3 transcription.

Knockout of S1P and S1P inhibitor prevent OVX-induced bone loss

Given the positive role of S1P in osteoclastogenesis, we were interested in whether S1P deficiency would protect the mouse from OVX-induced osteoporosis. Micro-CT analysis showed that S1P deficiency alleviated OVX-induced bone loss compared with the wild-type littermates (Fig. 7A, B). H&E staining of the femurs confirmed the micro-CT results (Supplementary Fig. S7A). TRAP staining showed S1P cKO mice had fewer osteoclasts on the trabecular surface of the femur compared with wild-type mice in the sham and OVX groups (Fig. 7C). Histomorphometric parameters of S1P-deficent femurs showed decrease in N.Oc/BS and Oc. S/BS compared with wild-type littermates in the sham and OVX groups (Fig. 7D). Further, we proposed S1P as a potential target for the treatment of bone loss. To this end, we treated mice with PF429242 for 8 weeks following OVX operation (Supplementary Fig. S7B). Micro-CT showed the values of BV/ TV and Tb.N were significantly increased while Tb.Sp was decreased in the PF429242-treated group (Fig. 7E, F). Furthermore, the protective effect of PF429242

on OVX-induced bone loss was confirmed by histological analysis, including TRAP staining and H&E (Fig. 7G and Supplementary Fig. S7C). In addition, the N.Oc/BS and Oc. S/BS were reduced in the PF429242 treatment group, but elevated in the vehicle group (Fig. 7G, H). In conclusion, knockout of S1P and S1P inhibitor prevented OVX-induced osteoporosis.

Knockout of S1P and S1P inhibitor protect mice from LPS-induced osteolysis

We had shown that suppressing S1P could extenuate chronic pathological bone loss. Here, we investigated whether S1P deficiency has a protective effect on acute osteolysis. The mice were injected once with 25 mg/kg LPS across the calvarial sagittal midline suture, under the skull periosteum and treated with PF429242 for 2 weeks following LPS injection (Supplementary Fig. S7D). As expected, the LysM-Cre-S1P[f/f] mice displayed less porosity and osteolysis (Fig. 8A, B). H&E staining showed S1P-deficent mice had more smooth and complete skull structure, whereas wild-type mice had severe osteolysis. In addition, TRAP staining showed less osteoclast activity following inflammation stimulation in the LysM-Cre-S1P[f/f] mice (Fig. 8C, D). Consistently, PF429242 treatment reduced porosity and osteolysis compared with the vehicle group (Fig. 8E, F). Also, H&E and TRAP staining showed that treatment with PF429242 reduced osteolysis and osteoclast activity under LPS stimulation (Fig. 8G, H). These data show that knockout of S1P and S1P inhibitor have a protective effect on acute osteolysis in vivo.

Discussion

S1P is a critical protease for activating unique membrane-bound latent transcription factors and is known as a key factor in various biological processes. Recently, S1P has been associated with skeleton development [18], and patient with S1P mutation exhibits skeletal dysplasia [19]. However, the role of S1P in osteoclastogenesis remains unclear. We showed here that S1P regulates osteoclast formation and resorptive activity via ATF6/CHOP/LC3 and SREBP2/LC3 pathways.

We firstly demonstrated that knockout of S1P impeds both formation and function of osteoclasts, while overexpression of S1P promoted osteoclastogenesis. We then constructed LyzM-Cre-S1P[f/f] and CTSK-Cre-S1P[f/f] mice to delete S1P specifically in the osteoclasts. The two models showed increased bone mass, which implied that S1P deficiency in osteoclast precursors, or late stage, could both damage osteoclasts resorption function in vivo. Increasing evidence had shown that S1P impacts on macrophage polarization by activating SREBP2, which sequentially promotes NLRP3
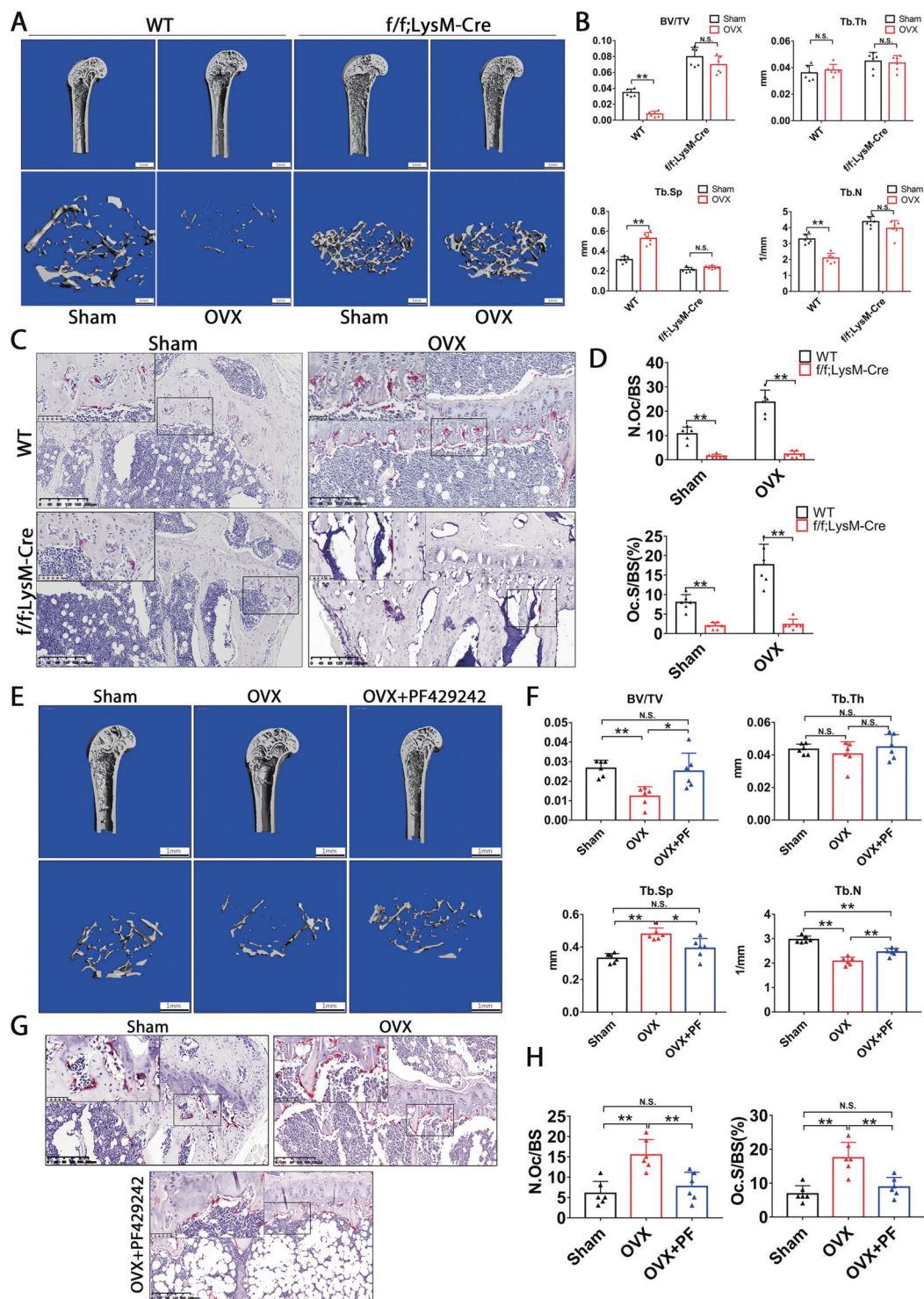
inflammasome activation [28]. Since NLRP3 inflammasome activation also plays critical role in osteoclastogenesis [29, 30], this study supports our results from another point of view. Interestingly, the knockout of S2P in macrophages doesn't affect NLRP3 inflammasome activation, which is consistent with our finding that S2P deficiency has no apparent influence on osteoclasts formation.

Based on the finding that S1P mRNA didn't increase in the induction of osteoclasts and OVX mice BMMs while S1P protein was upregulated, we proved miR-9-5p directly regulated S1P in osteoclasts. Consistently, it has been reported that reduced miR-9-5p raised osteoclasts survival, and regulated rheumatoid arthritis and inflammation by targeting NF-κB1 [21, 22, 31, 32]. It is to be expected that

◀ **Fig. 7 Knockout of S1P and S1P inhibitor prevent OVX-induced bone loss. A** Micro-CT and three-dimensional reconstructed images of distal femurs from WT or LysM-Cre-S1P$^{f/f}$ mice that underwent either sham or OVX operation. Scale bar, 1 mm. **B** Quantification of bone volume/tissue volume (BV/TV), trabecular number (Tb.N), trabecular separation (Tb.Sp) and trabecular thickness (Tb.Th) ($n = 6$). **C** TRAP staining of WT or LysM-Cre-S1P$^{f/f}$ mice femurs that underwent either sham or OVX operation; Scale bars, 200 μm. **D** Quantification of N. Oc/BS (osteoclast number/bone surface) and the percentage of osteoclast surface per bone surface (Oc.S/BS(%)) ($n = 6$). **E** Micro-CT and three-dimensional reconstructed images of distal femurs from sham and OVX mice injected with PBS or PF429242 for 2 months; Scale bar, 1 mm. **F** Quantification of bone volume/tissue volume (BV/TV), trabecular number (Tb.N), trabecular separation (Tb.Sp) and trabecular thickness (Tb.Th) ($n = 6$). **G** TRAP staining of the three groups mice femurs; Scale bars, 200 μm. **H** Quantification of N.Oc/BS (osteoclast number/bone surface) and the percentage of osteoclast surface per bone surface (Oc.S/BS(%)) ($n = 6$). Data are presented as mean ± SD. *$P < 0.05$, **$P < 0.01$. n value means the number of mice in each experiment.

miR-9-5p/S1P played important role in osteoclastogenesis. Autophagy is a complex process which requires smooth autophagy flux to function normally. It goes through the assemble of autophagosome, autolysosome fusion and substrate degradation [33]. Autophagy is crucial to the formation of osteoclasts. Osteoclastogenesis was inhibited when autophagy flux was blocked by Chloroquine treatment or by deletion of autophagy-related genes. LC3 is a critical component to the assemble of autophagosome and the transformation of LC3-I to LC3-II is used as a marker of autophagosome maturity. Knockout of LC3 suppressed F-actin formation, CTSK secretion and resorption activity of osteoclasts. During osteoclastogenesis, LC3 is transported to the ruffled border and this process is vital for the delivery of CTSK to the resorptive region [10, 11].

We detected the effects of S1P deficiency on BMMs and found that ER stress and apoptosis showed no significant changes, although autophagy flux appeared to be blunt. Particularly, LC3 was decreased in S1P-deficient BMMs following RANKL treatment, which showed a similar expression tendency as S1P. ATF6 and SREBP2, two classical substrates of S1P, were closely related to autophagy and LC3 expression. All these evidences strongly imply that the transcription of LC3 is directly regulated by S1P downstream signaling. Indeed, exogenous expression of LC3 in S1P-deficient BMMs evidently rescued osteoclast formation and resorptive activity, which suggests that S1P regulation of osteoclastogenes is LC3 dependent.

We confirmed that CHOP formed a complex with SREBP2 and directly binds to the promoter of LC3, and synergistically enhanced the transcriptional activity. To gain further insights into the interaction, we screened the naturally interaction regions by Co-immunoprecipitation and molecular docking. LZIP (S5) in SREBP2 and bZIP (C3) in CHOP were verified as critical domains for their interaction.

It should be noted that (Gln)-rich region (S3) in SREBP2 also showed interaction with CHOP by Co-immunoprecipitation, although the homology modeling was failed due to a lack of structure data.

To evaluate the therapeutic potential of targeting S1P in vivo, we constructed OVX- and LPS-induced osteolysis models. As expected, S1P deficiency could evidently reverse bone loss in OVX- and LPS-induced osteolysis. Intraperitoneal injection of the S1P inhibitor, PF429242, rescued the osteolysis which was caused by a lack of estrogen and by acute inflammation. However, more researches are required for clarifying whether PF429242 could reverse established damage. Regarding S1P deficiency also impeding osteoblastogenesis, it was interesting that PF429242 prevented osteolysis and increased bone mass in vivo. This could be because inhibition of osteoclastogenesis and inflammation by PF429242 contributes more benefit to bone mass compared with the side effect in OVX- and LPS-induced osteolysis. Nevertheless, the osteoclast-targeted drug delivery system should be utilized to ensure security and specific-targeting in further studies.

In conclusion, our study is the first to clarify how S1P controls osteoclastogenesis by affecting LC3 transcription via the ATF6/CHOP/LC3 and SREBP2/LC3 pathways. The rescue experiment in vivo implies that S1P can be a potential target for treatment of osteoporosis.

Materials and methods

Reagents

PF429242 (HY-13447A, MCE), Fatostatin (HY-14452, MCE). Alpha-MEM and FBS (fetal bovine serum) were obtained from Gibco. Recombinant mouse M-CSF (CB34, Novoprotein) and RANKL (462-TEC, R&D). Recombinant human M-CSF (C417, Novoprotein) and RANKL (390-TN-010, R&D). The osteoclasts were stained using TRAP (tartrate-resistant acid phosphatase) staining kits (387A-1KT, Sigma-Aldrich). Mouse PINP (Procollagen I N-Terminal Propeptide) ELISA Kit (E-EL-M0233c, Elabscience, China), Mouse CTX I (C-terminal telopeptide of type I collagen) ELISA Kit (E-EL-M0366c, Elabscience, China). Cycloheximide (0970/100, R&D). miR-9-5p inhibitor and mimic (Ribobio, Shanghai, China).

Mice

S1P flox/flox mice were provided by Prof. Di Wang (Institute of Immunology, Zhejiang University School of Medicine, China), LysM-Cre mice were provided by Model Animal Research Center of Nanjing University, and CTSK-Cre mice were provided by Prof. Shigeaki Kato (Institute of Molecular
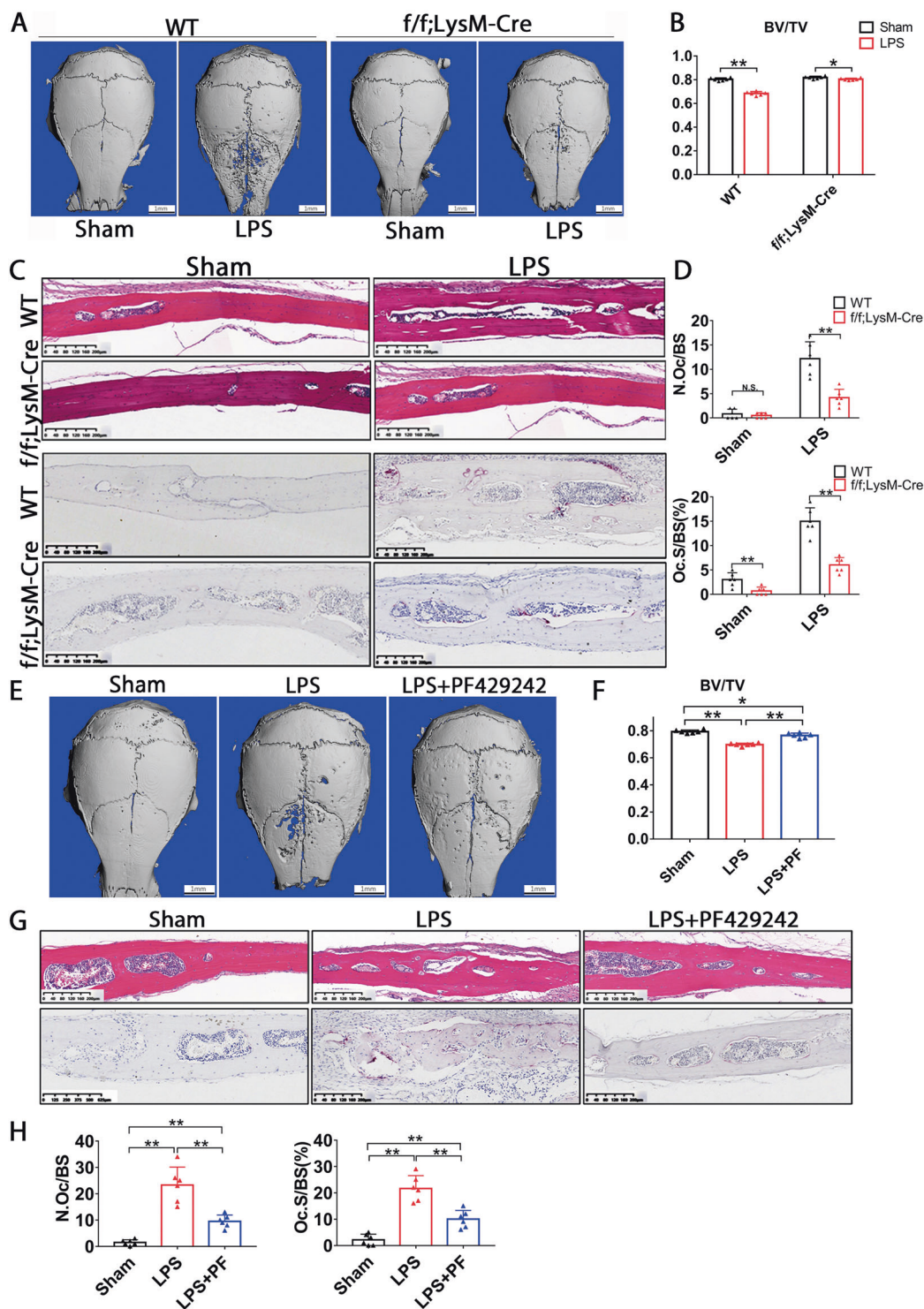
Fig. 8 Knockout of S1P and S1P inhibitor protect mice from LPS-induced osteolysis. A Micro-CT and three-dimensional reconstructed images of calvaria WT or LysM-Cre-S1P$^{f/f}$ mice injected with LPS or sham operation; Scale bar, 1 mm. **B** Quantification of bone volume/tissue volume (BV/TV) ($n = 6$). **C** H&E and TRAP staining of calvaria from WT or LysM-Cre-S1P$^{f/f}$ mice injected with LPS or sham operation; Scale bars, 200 μm. **D** Quantification of N.Oc/BS (osteoclast number/bone surface) and the percentage of osteoclast surface per bone surface (Oc.S/BS(%)) ($n = 6$). **E** Micro-CT and three-dimensional reconstructed images of calvarial from sham-operated mice (control), and LPS mice injected with PBS or PF429242; Scale bar, 1 mm. **F** Quantification of bone volume/tissue volume (BV/TV) ($n = 6$). **G** H&E and TRAP staining of calvaria from the three groups mice; Scale bars, 200 μm. **H** Quantification of N.Oc/BS (osteoclast number/bone surface) and the percentage of osteoclast surface per bone surface (Oc.S/BS(%)) ($n = 6$). Data are presented as mean ± SD. *$P < 0.05$, **$P < 0.01$. n value means the number of mice in each experiment.

and Cellular Biosciences, University of Tokyo, Japan). In all experiments, LysM-Cre-S1P[f/f] or CTSK-Cre-S1P[f/f] mice were compared with their WT littermates (S1P[f/f]). All animal studies were approved by the Ethics Committee of Sir Run Run Shaw Hospital, Zhejiang University School of Medicine.

μ-CT analysis

For μ-CT analysis, 3-month-old mouse distal femurs were scanned by the μ-CT scanner (Skyscan 1072, Aartselaar, Belgium) using the X-ray energy of $80\,\mu A/70\,kV$ and the isometric resolution of 9 μm. The scan of the trabecular bone was performed from the growth plate, and consisted of 130 slices were analyzed for the BV/TV (trabecular bone volume per total volume), Tb.Th (trabecular thickness), Tb.Sp (trabecular separation), and Tb.N (trabecular number) using the CT Evaluation Program, as described previously [34].

Histology

The fixed femurs of mice were decalcified in 12% EDTA2Na at room temperature for ~2 weeks and embedded in paraffin. The slices were used for TRAP staining, H&E (hematoxylin and eosin) staining, and immunohistochemical staining. The osteoclast numbers per bone surface (N.Oc/BS) and osteoclast covered surface per bone surface (Oc.S/BS) were assessed by a microscope.

Cell culture and osteoclasts differentiation

HEK-293T cells was obtained from National Collection of Authenticated Cell Cultures, Chinese Academy of Sciences. The cell line was determined to be free of mycoplasma contamination by PCR and culture. Their species origins were confirmed using PCR. The identity of the cell line was authenticated with STR profiling. The murine BMMs (bone marrow monocytes) were isolated as described previously [34]. Briefly, the BMMs were isolated from the femurs and tibias of C57BL/6 mice and cultured with 10% FBS, alpha-MEM, 1% penicillin/streptomycin, 25 ng/ml M-CSF and 50 ng/ml RANKL under 5% CO_2, 37 °C. The human PBMs (peripheral blood monocytes) were isolated according to the protocol of Ficoll separation liquid (P9011, Solarbio). Briefly, the PBMs were isolated from human peripheral blood of volunteers and cultured with 10% FBS, alpha-MEM, 1% penicillin/streptomycin, 25 ng/ml M-CSF and 50 ng/ml RANKL under 5% CO_2, 37 °C. Multinucleated osteoclasts that were induced for 5 days (BMMs) or 12 days (PBMs) were immediately fixed in 4% paraformaldehyde for 30 min at room temperature and stained in TRAP solution for 1 h at 37 °C. The present study was approved by the Ethics Committee of Sir Run Run Shaw Hospital, Zhejiang University School of Medicine and all volunteers signed a consent form.

Bone resorption assay

The hydroxyapatite resorption assay was performed as described previously [35]. BMMs were isolated from the femurs and tibias of C57BL/6 mice and after 4 days cultured with 25 ng/ml M-CSF, the BMMs were seeded into each well of hydroxyapatite-coated plate (3989, Corning Inc., USA). Cells were treated with 25 ng/ml M-CSF and 50 ng/ml RANKL. After 72 h incubation, the wells were washed with 10% sodium hypochlorite to remove cells. Then we used the microscope to capture the images of hydroxyapatite resorption areas and quantified these by using Image J software.

The proliferation and apoptosis assay

The cytotoxicity of deficiency on BMMs was detected using the CCK-8 assay. The BMMs were seeded in 96-well plates (1.5×10^4 cells/well) with 25 ng/ml M-CSF and cultured for 72 h. Afterward, a 10-μl CCK-8 buffer (K1018, APExBIO, USA) was added to each well. All plates were incubated at 37 °C for an additional 1 h. Absorbance of 450 nm wavelength was detected using the Multiscan Go (Thermo Scientific). For apoptosis detection, BMMs were isolated from WT mice and LysM-Cre-S1P[f/f] mice and cultured with 25 ng/ml M-CSF for 3 days. Then the BMMs were gently dissociated by pancreatin without EDTA and detected by PE Annexin V apoptosis detection kit (BD Biosciences, San Diego, CA, United States). Flow cytometric analysis was performed using a Gallios flow cytometer and Kaluza analysis software (Beckman Coulter).

siRNAs transfection

BMMs were transfected with siRNA as described previously [34]. BMMs were plated in 6, 12 or 96-well plates with 25 ng/ml M-CSF for 24 h and then transfected with siRNAs (Ribobio, Shanghai, China) using Lipofectamine™ 3000 Transfection Reagent (2078159, Invitrogen) according to the instructions. The cultured medium was replaced after 24 h siRNA transfecting. The siRNA sequences for mouse S2P-siRNA-1 (Sequence: 5′-GCAGCUAUUAGGGAACA AGUU-3′), S2P-siRNA-2 (Sequence: 5′-CCAGUGAUUG UGGAGACAUUU-3′), SREBP2-siRNA-1 (Sequence: 5′-GCGGACAACACACAAUAUCAU-3′), SREBP2-siRNA-2 (Sequence: 5′-GAUGCUACAGUUUGUCAGCAA-3′).

Western blot analysis

BMMs were plated (3×10^5 cells/well) in 6-well plates. Cells were cultured with 25 ng/ml M-CSF, with or without 50 ng/ml RANKL. The proteins were extracted from the cells using RIPA (Solar bio, Beijing, China) mixed with

100×Phosphatase Inhibitor Cocktail (CWBIO, China), 100 mM phenylmethanesulfonyl fluoride (Beyotime, Zhengzhou, China), and Protease Inhibitor Cocktail (Millipore, USA). The extract was centrifugated at 12000 rpm for 15 min and the supernatants were heated at 100 °C for 10 min. SDS–polyacrylamide gel electrophoresis were performed according to the formerly protocol [34]. The bands were detected by Amersham Imager 600 (GE, USA). The images were quantified by Image J. Western blot was performed using following antibodies: S1P Rabbit pAb (A16243, ABclonal, 1:1000), NFATC1 Mouse mAb (sc-7294, Santa Cruz, 1:1000), ATF6 Mouse mAb (sc-166659, Santa Cruz, 1:1000), CHOP Rabbit pAb (ET1703-05, HUABIO, 1:1000), PERK Rabbit mAb (ab229912, Abcam, 1:1000), BiP Rabbit mAb (3177, Cell Signaling Technology, 1:1000), XBP-1 Mouse mAb (sc-8015, Santa Cruz, 1:1000), ATF4 Rabbit mAb (ET1612-37, HUABIO, 1:1000), LC3 Rabbit pAb (2775, Cell Signaling Technology, 1:1000), SQSTM1 Rabbit mAb (39749, Cell Signaling Technology, 1:1000), SREBP2 Rabbit pAb (ab30682, Abcam, 1:1000), S2P Rabbit pAb (BS61210, Bioworld, 1:1000), GAPDH Mouse mAb (AC002, ABclonal, 1:1000), EDEM1 Rabbit pAb (ER60701, HUABIO, 1:1000), CANX Rabbit pAb (ER1803-43, HUABIO, 1:1000), ERN1 Mouse mAb (SC-390960, Santa Cruz, 1:1000), DNAJB9 Rabbit pAb (A7494, abclonal, 1:1000).

RNA extraction and quantitative PCR

The cells were seeded (2×10^5 cells/well) in 12-well plates and cultured with 25 ng/ml MCSF overnight. BMMs were then stimulated with 50 ng/ml RANKL for 5 days. mRNA was generated using Ultrapure RNA Kit (CW0581, CWBIO, China) according to the manufacturers' protocols. mRNA reverse transcription was performed using HiFi-Script cDNA Synthesis kit (CW2569, CWBIO, China). RT-qPCR quantification was performed using UltraSYBR Mixture (CW0957, CWBIO, China) according to the manufacturers' protocols. The relative mRNA expression levels were normalized to the GAPDH expression levels. The primer sequences used in this study are presented in Supplementary Fig. S8A. miRNA reverse transcription was performed using Mir-X miRNA First-Strand Synthesis Kit (638315, TAKARA, Japan). The relative miRNA expression levels were normalized to the U6 expression levels.

Chromatin immunoprecipitation (ChIP)

BMMs were cultured in the presence or absence of 50 ng/ml RANKL for 3 days. After incubation, cells were fixed in 37% formaldehyde for 10 min at room temperature. ChIP assay was performed using the ChIP assay kit (9002, Cell Signaling Technology) according to the manufacturers' protocols. The immunoprecipitated DNA fragments were collected for PCR amplification. The nucleotide sequences of the oligos used in the assay are presented in Supplementary Fig. S8B.

Luciferase reporter assay

Briefly, the HEK-293T cells were transfected with a vector or specific gene-luc (Vigene, Shandong, China) with Renilla (Promega). Luciferase activity was measured using the dual luciferase reporter assay kit (Beyotime, Shanghai, China). Transcriptional activity was measured as the ratio of firefly/Renilla luciferase activity.

Cellular immunofluorescent staining

For F-actin ring staining, the matured osteoclasts were then fixed in 4% paraformaldehyde, permeabilized in 0.15% Triton X-100, washed in PBS, and immunostained with phalloidin (Servicebio). For anti-LC3 immunofluorescence stain, osteoclasts on 6-well slides were fixed by 4% paraformaldehyde for half an hour, permeabilized with 0.15% Triton X-100, blocked with 5% bovine serum albumin in PBS, the cells were incubated with LC3 primary antibodies (RT1359, 1:100, HUABIO), SREBP2 primary antibodies (sc-13552, Santa Cruz, 1:100) or CHOP primary antibodies (A0221, Abclonal, 1:100) overnight at 4 °C. Then the cells were incubated with secondary antibodies: Goat Anti-Rabbit IgG H&L (Alexa Fluor 488) (ab150077, Abcam, 1:500) or Goat Anti-Mouse IgG H&L (Alexa Fluor 488) (ab150113, Abcam, 1:500) in PBS for 30 min after washing with PBST. The images were taken by confocal microscopy (Nikon Eclipse Ti Japan).

Co-immunoprecipitation (IP) assay

The HEK-293T cells were divided into three groups and transfected with specific gene plasmid for 48 h. Then cells were immersed in lysis buffer supplemented with 1 mM PMSF, 1 mM dithiothreitol (DTT), and Protease Inhibitor Cocktail. Cell lysates were immunoprecipitated with anti-Flag (14793, Cell Signaling Technology) antibody or anti-Myc (EM31105, HUABIO) antibody at 4 °C overnight, then incubated with protein A/G-beads for 3 h at 4 °C. The complexes were washed five times in PBS supplemented with Protease Inhibitor Cocktail at 4 °C, resolved by 10% SDS-PAGE and then analyzed by western blotting.

Homology modeling and molecular docking

The structure of CHOP (positions 101–160) was conducted by homology modeling using SWISS-MODEL webserver [36–40]. Crystal structure of SREBP2 was obtained from RCSB Protein Database Bank (PDB code: 1UKL, chain C

and chain D). The structures of the biopolymers were analyzed and prepared for the docking experiment. Hydrogen atoms with H-bond orientation were added. All ligands and water molecules were removed, the relevant side-chains were repaired and the bumps were fixed. Docking study of the binding mode between the CHOP and SREBP2 was conducted by ZDock webserver [41]. The results of the binding mode were mapped with PYMOL program (http://www.pymol.org/).

Ovariectomy (OVX)-induced osteoporosis model

OVX-induced osteoporosis model was established as previously described [34]. Sham or OVX operation was performed on 12-week-old female C57BL/6 mice. The mice were randomly divided into three groups: the sham group, the OVX with saline injection group, and the OVX with PF429242 injection group. Saline or PF429242 (3 mg/kg) was injected twice a week for 2 months. All the mice were sacrificed 2 months after operation. Femurs and tibiae were gathered and fixed in 4% paraformaldehyde for μ-CT and bone histomorphometry analysis.

LPS-induced calvarial osteolysis model

LPS-induced calvarial osteolysis was performed on 12-week-old male C57BL/6 mice. The mice were randomly divided into three groups: the sham group, the LPS-induced with PBS injection group, and the LPS-induced with PF429242 injection group. The mice were subcutaneously injected with 25 mg/kg LPS (L2880, Sigma-Aldrich) once and then PBS or PF429242 (3 mg/kg) was injected every two days for 2 weeks. All the mice were sacrificed 2 weeks after operation. Craniums were gathered and fixed in 4% paraformaldehyde for μ-CT and bone histomorphometry analysis.

Collagen induced arthritis (CIA) model

Sham or collagen induced arthritis were performed on 8-week-old male DBA/1 mice according to Chondrex protocol. Chick type II collagen solution (20011, Chondrex, USA) (4 mg/ml in 0.05 M acetic acid) was mixed with Complete Freund's Adjuvant (7001, Chondrex, USA) in equal volume and the mixture was emulsificated using ultrasonic crusher. Insert the 25 gauge needle bevel side up and parallel to the tail at 2 cm from the base of the tail until the needle tip reaches 0.5 cm from the base and inject 100ul of the emulsion. After 21 days, Chick type II collagen solution was mixed with Incomplete Freund's Adjuvant (7002, Chondrex, USA) in equal volume and emulsificated. For a booster injection, insert the needle at 3 cm from the base of the tail until the tip reaches 1.5 cm from the base. The mice were sacrificed 14 days after the twice injection.

Statistical analysis

The data represented mean ± S.D. Data analysis was performed using SPSS 19.0 (SPSS, Chicago). Sample size was estimated empirically, according to the exploratory experiments and published literatures with similar methodology. When applicable (methodology based) investigators were blinded for the condition. Statistical differences were analyzed by two-tailed Student's t test or one-way ANOVA followed by Tukey's post hoc analyses where appropriate. Values represent mean ± S.D. Variance between groups statistically compared was similar. As indicated in the figure legend, P value ≤ 0.05 was considered statistically significant.

Data and materials availability

All data needed to evaluate the conclusions in the paper are present in the paper and/or the Supplementary Materials. Additional data related to this paper may be requested from the authors.

Author contributions ZZ, XZ, BH, JL, XW, and ZS performed the experiments, analyzed the data and edited the manuscript. HW, ZF, and YC performed mice experiments and revised the manuscript. SF conceived the project and revised the manuscript. FZ and JC conceived the project, designed the experiments and edited the manuscript. All authors discussed the results and contributed to the preparation of the manuscript.

Compliance with ethical standards

Ethics statement Ethical approval was obtained from Medical Ethics Committee of the author's hospital.

Conflict of interest The authors declare that they have no conflict of interest.

Publisher's note Springer Nature remains neutral with regard to jurisdictional claims in published maps and institutional affiliations.

References

1. Harada S, Rodan GA. Control of osteoblast function and regulation of bone mass. Nature. 2003;423:349–55.
2. Teitelbaum SL. Bone resorption by osteoclasts. Science. 2000; 289:1504–8.

3. McInnes IB, Schett G. Cytokines in the pathogenesis of rheumatoid arthritis. Nat Rev Immunol. 2007;7:429–42.

4. Veletic I, Manshouri T, Multani AS, Yin CC, Chen L, Verstovsek S, et al. Myelofibrosis osteoclasts are clonal and functionally impaired. Blood. 2019;133:2320–4.

5. Compston JE, McClung MR, Leslie WD. Osteoporosis. Lancet. 2019;393:364–76.

6. Klionsky DJ. Autophagy: from phenomenology to molecular understanding in less than a decade. Nat Rev Mol Cell Biol. 2007; 8:931–7.

7. Mizushima N, Yoshimori T, Levine B. Methods in mammalian autophagy research. Cell. 2010;140:313–26.

8. Zhao Y, Chen G, Zhang W, Xu N, Zhu JY, Jia J, et al. Autophagy regulates hypoxia-induced osteoclastogenesis through the HIF-1alpha/BNIP3 signaling pathway. J Cell Physiol. 2012;227:639–48.

9. Wang K, Niu J, Kim H, Kolattukudy PE. Osteoclast precursor differentiation by MCPIP via oxidative stress, endoplasmic reticulum stress, and autophagy. J Mol Cell Biol. 2011;3:360–8.

10. DeSelm CJ, Miller BC, Zou W, Beatty WL, van Meel E, Takahata Y, et al. Autophagy proteins regulate the secretory component of osteoclastic bone resorption. Dev Cell. 2011;21:966–74.

11. Chung YH, Yoon SY, Choi B, Sohn DH, Yoon KH, Kim WJ, et al. Microtubule-associated protein light chain 3 regulates Cdc42-dependent actin ring formation in osteoclast. Int J Biochem Cell Biol. 2012;44:989–97.

12. Lin NY, Chen CW, Kagwiria R, Liang R, Beyer C, Distler A, et al. Inactivation of autophagy ameliorates glucocorticoid-induced and ovariectomy-induced bone loss. Ann Rheum Dis. 2016;75:1203–10.

13. Lin NY, Beyer C, Giessl A, Kireva T, Scholtysek C, Uderhardt S, et al. Autophagy regulates TNFalpha-mediated joint destruction in experimental arthritis. Ann Rheum Dis. 2013;72:761–8.

14. Ye J, Rawson RB, Komuro R, Chen X, Davé UP, Prywes R, et al. ER stress induces cleavage of membrane-bound ATF6 by the same proteases that process SREBPs. Mol Cell. 2000;6:1355–64.

15. Wang X, Sato R, Brown MS, Hua X, Goldstein JL. SREBP-1, a membrane-bound transcription factor released by sterol-regulated proteolysis. Cell. 1994;77:53–62.

16. Yang J, Goldstein JL, Hammer RE, Moon YA, Brown MS, Horton JD. Decreased lipid synthesis in livers of mice with disrupted Site-1 protease gene. Proc Natl Acad Sci USA. 2001;98:13607–12.

17. Achilleos A, Huffman NT, Marcinkiewicyz E, Seidah NG, Chen Q, Dallas SL, et al. MBTPS1/SKI-1/S1P proprotein convertase is required for ECM signaling and axial elongation during somitogenesis and vertebral developmentdagger. Hum Mol Genet. 2015;24:2884–98.

18. Patra D, Xing X, Davies S, Bryan J, Franz C, Hunziker EB, et al. Site-1 protease is essential for endochondral bone formation in mice. J Cell Biol. 2007;179:687–700.

19. Kondo Y, Fu J, Wang H, Hoover C, McDaniel JM, Steet R, et al. Site-1 protease deficiency causes human skeletal dysplasia due to defective inter-organelle protein trafficking. JCI Insight. 2018;3: e121596.

20. Wu M, Chen W, Lu Y, Zhu G, Hao L, Li YP. Galpha13 negatively controls osteoclastogenesis through inhibition of the Akt-GSK3beta-NFATc1 signalling pathway. Nat Commun. 2017;8:13700.

21. Lee WS, Yasuda S, Kono M, Kudo Y, Shimamura S, Kono M, et al. MicroRNA-9 ameliorates destructive arthritis through down-regulation of NF-κB1-RANKL pathway in fibroblast-like synoviocytes. Clin Immunol. 2020;212:108348.

22. Wang S, Tang C, Zhang Q, Chen W. Reduced miR-9 and miR-181a expression down-regulates Bim concentration and promote osteoclasts survival. Int J Clin Exp Pathol. 2014;7:2209–18.

23. Zinszner H, Kuroda M, Wang X, Batchvarova N, Lightfoot RT, Remotti H, et al. CHOP is implicated in programmed cell death in response to impaired function of the endoplasmic reticulum. Genes Dev. 1998;12:982–95.

24. Wang J, Kang R, Huang H, Xi X, Wang B, Wang J, et al. Hepatitis C virus core protein activates autophagy through EIF2AK3 and ATF6 UPR pathway-mediated MAP1LC3B and ATG12 expression. Autophagy. 2014;10:766–84.

25. Zheng ZG, Cheng HM, Zhou YP, Zhu ST, Thu PM, Li HJ, et al. Dual targeting of SREBP2 and ERRalpha by carnosic acid suppresses RANKL-mediated osteoclastogenesis and prevents ovariectomy-induced bone loss. Cell Death Differ. 2020;27: 2048–65.

26. Inoue K, Imai Y. Fatostatin, an SREBP inhibitor, prevented RANKL-induced bone loss by suppression of osteoclast differentiation. Biochim Biophys Acta. 2015;1852:2432–41.

27. Seo YK, Jeon TI, Chong HK, Biesinger J, Xie X, Osborne TF. Genome-wide localization of SREBP-2 in hepatic chromatin predicts a role in autophagy. Cell Metab. 2011;13:367–75.

28. Guo C, Chi Z, Jiang D, Xu T, Yu W, Wang Z, et al. Cholesterol homeostatic regulator SCAP-SREBP2 integrates NLRP3 inflammasome activation and cholesterol biosynthetic signaling in macrophages. Immunity. 2018;49:842–56. e847

29. Zang Y, Song JH, Oh SH, Kim JW, Lee MN, Piao X, et al. Targeting NLRP3 inflammasome reduces age-related experimental alveolar bone loss. J Dent Res. 2020;99:1287–95.

30. Qu C, Bonar SL, Hickman-Brecks CL, Abu-Amer S, McGeough MD, Peña CA, et al. NLRP3 mediates osteolysis through inflammation-dependent and -independent mechanisms. FASEB J. 2015;29:1269–79.

31. Yue P, Jing L, Zhao X, Zhu H, Teng J. Down-regulation of taurine-up-regulated gene 1 attenuates inflammation by sponging miR-9-5p via targeting NF-κB1/p50 in multiple sclerosis. Life Sci. 2019;233:116731.

32. Bazzoni F, Rossato M, Fabbri M, Gaudiosi D, Mirolo M, Mori L, et al. Induction and regulatory function of miR-9 in human monocytes and neutrophils exposed to proinflammatory signals. Proc Natl Acad Sci USA. 2009;106:5282–7.

33. Levine B, Kroemer G. Biological functions of autophagy genes: a disease perspective. Cell. 2019;176:11–42.

34. Xie Z, Yu H, Sun X, Tang P, Jie Z, Chen S, et al. A novel diterpenoid suppresses osteoclastogenesis and promotes osteogenesis by inhibiting Ifrd1-mediated and IkappaBalpha-mediated p65 nuclear translocation. J Bone Min Res. 2018;33:667–78.

35. Chen K, Qiu P, Yuan Y, Zheng L, He J, Wang C, et al. Pseurotin A inhibits osteoclastogenesis and prevents ovariectomized-induced bone loss by suppressing reactive oxygen species. Theranostics. 2019;9:1634–50.

36. Guex N, Peitsch MC, Schwede T. Automated comparative protein structure modeling with SWISS-MODEL and Swiss-PdbViewer: a historical perspective. Electrophoresis. 2009;30:S162–173.

37. Bertoni M, Kiefer F, Biasini M, Bordoli L, Schwede T. Modeling protein quaternary structure of homo- and hetero-oligomers beyond binary interactions by homology. Sci Rep. 2017;7:10480.

38. Studer G, Rempfer C, Waterhouse AM, Gumienny R, Haas J, Schwede T. QMEANDisCo-distance constraints applied on model quality estimation. Bioinforma. 2020;36:2647.

39. Bienert S, Waterhouse A, de Beer TA, Tauriello G, Studer G, Bordoli L, et al. The SWISS-MODEL repository-new features and functionality. Nucleic Acids Res. 2017;45:D313–d319.

40. Waterhouse A, Bertoni M, Bienert S, Studer G, Tauriello G, Gumienny R, et al. SWISS-MODEL: homology modelling of protein structures and complexes. Nucleic Acids Res. 2018;46: W296–w303.

41. Pierce BG, Wiehe K, Hwang H, Kim BH, Vreven T, Weng Z. ZDOCK server: interactive docking prediction of protein-protein complexes and symmetric multimers. Bioinforma. 2014;30:1771–3.